Global and Planetary Change 228 (2023) 104214

Contents lists available at ScienceDirect

Global and Planetary Change

journal homepage: www.elsevier.com/locate/gloplacha

Mercury isotopes record development and attenuation of photic zone euxinia during the earliest Cambrian

Kun Zhao [a], Guangyou Zhu [b,*], Wang Zheng (郑旺)[c], Guangyi Sun [d], Tingting Li [b], Zhiyao Zhang [e]

[a] Institute of Sedimentary Geology, Chengdu University of Technology, Chengdu 610059, China
[b] Research Institute of Petroleum Exploration and Development, PetroChina, Beijing 100083, China
[c] Institute of Surface-Earth System Science, School of Earth System Science, Tianjin University, Tianjin 300072, China
[d] State Key Laboratory of Environmental Geochemistry, Institute of Geochemistry, Chinese Academy of Sciences, Guiyang 550081, China
[e] School of Earth Resources, China University of Geosciences, Wuhan 430074, China

ARTICLE INFO

Editor: Dr. Maoyan Zhu

Keywords:
Photic zone euxinia
Mercury isotopes
Carbon isotopes
Early Cambrian
Tarim basin

ABSTRACT

The Ediacaran-Cambrian transition period (ca. 550–521 Ma) witnessed the decline of Ediacaran Biota and the rapid diversification of Cambrian biota. Numerous studies have linked the biological evolution to redox conditions in the early Cambrian ocean, which are still strongly debated. Photic zone euxinia (PZE), characterized by the development of anoxic conditions and build-up of free hydrogen sulfide (H_2S) in the photic zone, would have seriously challenged the survival of early organisms and have been proposed to cause several extinctions. However, this potentially deleterious environmental condition has not been recognized at the Ediacaran – Cambrian boundary. Here, we analyzed mercury (Hg) contents and stable isotopes, carbon isotopes ($\delta^{13}C_{carb}$ and $\delta^{13}C_{org}$), and organic carbon contents (TOC) from drill core recovered from the Tarim Basin, to constrain the potential impact of PZE in the earliest Cambrian ocean. A significant negative shift in Hg mass-independent isotope fractionation (MIF) is recorded in the basal Cambrian negative carbon isotope excursion (BACE) of the Yurtus Formation, combined with similar Hg isotope compositions in the Yangtze area (Tongren section), suggesting that the photoreduction of Hg(II) associated with the regional development of the PZE during the earliest Cambrian. Integrated with biotic records, our results suggest that the development of PZE in the earliest Cambrian ocean may have significantly limited habitable space. Instead, the attenuation of PZE could restore aerobic photosynthesis by removing H_2S, creating a suitable habitat for the diversification of early animals.

1. Introduction

The Ediacaran-Cambrian transition period (ca. 550–521 Ma) represents a milestone in geologic history with remarkable biological innovations and changes in the marine environment. This interval witnessed both the decline of soft-bodied and skeletal Ediacaran-type biota and the rapid appearance and diversification of the Cambrian-type skeletal biota (Bowyer et al., 2023; Wood et al., 2019; Zhu et al., 2017). Despite the notable biologic changes over this period, however, its predominant triggers remain unclear, especially the disappearance of largely Ediacaran-type biota approximately coincident with the BACE, which has been proposed to reflect a potential biotic crisis (Amthor et al., 2003; Laflamme et al., 2013; Zhu et al., 2006). Previous studies have linked these biotic transitions to environmental changes, suggesting that rising environmental oxygen levels facilitated early animal evolution (Canfield et al., 2007; Wood et al., 2019; Zhang et al., 2019), which is based on the basic assumption that early animals required oxygen to maintain aerobic metabolism. Besides, there are also other possible explanations for this biotic transition, such as genetic and developmental possibility, ecological opportunities (see details in Erwin et al., 2011). Although numerous studies have attributed the large decline in the diversity of the Ediacaran-type biota to widespread anoxia in the terminal Ediacaran (Zhang et al., 2018, 2019), yet new $\delta^{238}U$ data and biotic records from the Lower Nama Group (ca. 550–547 Ma), Namibia, argue that the global expansion of anoxia did not coincide with the decline of the Ediacaran biota (Tostevin et al., 2019). Indeed, a global redox landscape in the Ediacaran – Cambrian transition periods has been proposed, that is highly dynamic, with brief ocean oxygenation events, redox-stratified shelf, and an anoxic-dominated deep ocean (Li et al., 2020; Tostevin et al., 2016; Tostevin and Mills, 2020; Wood et al.,

* Corresponding author.
E-mail address: zhuguangyou@petrochina.com.cn (G. Zhu).

https://doi.org/10.1016/j.gloplacha.2023.104214
Received 31 March 2023; Received in revised form 19 July 2023; Accepted 13 August 2023
Available online 14 August 2023

2015). It is now generally accepted that the evolution of early animals was closely linked to changes in the marine environment, such as nutrient supply and oxygen availability (He et al., 2019; Tostevin et al., 2016; Wood et al., 2015). Furthermore, a habitable marine redox condition is conducive to the survival of early animals, instead, an inhospitable marine environment (e.g., photic zone euxinia) would severely restrict the survival space of early animals.

Photic zone euxinia refers to anoxic and H_2S-rich waters in the photic zone (Zheng et al., 2018). Prevalent PZE in the oceans would severely threaten habitability for eukaryotic organisms and delay the evolution of early animals (Grice et al., 2005). In particular, PZE generally directly affects photosynthesis by poisoning photosystem II (PSII, a unit of photosynthesis) (Oren et al., 1979), and influences organic carbon burial and atmospheric oxidation. On one hand, extensively developed passive continental margins are more receptive to increased nutrient inputs through enhanced continental weathering and PO_4^{3-}-enriched deep water upwelling, and, therefore, probably created favorable conditions for the development of PZE. On the other hand, the large disappearance of Ediacaran-type biota during the Ediacaran-Cambrian transition periods probably due to the shrink of habitat space, which the development of PZE maybe a potential environment trigger factor. Instead, the attenuation of PZE could re-establish aerobic photosynthesis by removing H_2S, creating a suitable habitat for the diversification of early animals. Therefore, recognizing the development of PZE in the geological past is critical to understanding the intrinsic link between the marine environment and biological radiation.

In recent years, mercury (Hg) and its stable isotope compositions in sedimentary rocks have shown unique advantages in recording ancient volcanic activity and oceanic redox state and have demonstrated great potential in reconstructing Earth's paleo-environment evolution (Bergquist, 2017; Fan et al., 2020; Grasby et al., 2019; Sial et al., 2013). Mercury has seven stable isotopes (^{196}Hg, ^{198}Hg, ^{199}Hg, ^{200}Hg, ^{201}Hg, ^{202}Hg, and ^{204}Hg), and their natural abundances are 0.155, 10.04, 16.94, 23.14, 13.17, 29.73, and 6.82, respectively (Blum and Bergquist, 2007). Mercury can undergo a variety of isotopic fractionation due to its chemical properties, including mass dependent fractionation (MDF), odd-mass independent fractionation (odd MIF, denote Δ^{199}Hg and Δ^{201}Hg), and even-mass independent fractionation (even MIF, denote Δ^{200}Hg and Δ^{204}Hg) (Blum et al., 2014). Hg-MDF occurs in most physical, chemical, and biological processes (Blum et al., 2014), whereas Hg-MIF primarily occurs in photochemical processes (Bergquist and Blum, 2007; Blum et al., 2014). Thus Hg-MIF could provide conservative and precise information regarding Hg sources and processes. Studies of Hg isotope compositions in modern and ancient Hg reservoirs suggest that the volcanic and hydrothermal sources of Hg have near-zero Δ^{199}Hg and Δ^{200}Hg values (Blum et al., 2014; Grasby et al., 2017; Sial et al., 2013). In contrast, modern seawater and some ancient sedimentary rocks record positive Hg-MIF signals (Grasby et al., 2019), which were typically interpreted to indicate photoreduction of Hg(II) species in the atmosphere and/or in the surface ocean (Štrok et al., 2015). The modern terrestrial reservoirs are generally characterized by negative Δ^{199}Hg and Δ^{200}Hg values (Zheng et al., 2016), due to the uptake of atmospheric gaseous Hg(0) by plants and soil organic matter. However, significantly negative Hg-MIF values were also observed in sedimentary rocks in the absence of terrestrial biomass (e.g. in the Mesoproterozoic period), which were ascribed to photoreduction of Hg(II) associated with reduced sulfur ligands under PZE conditions (Zheng et al., 2018). This suggests that Hg stable isotopic compositions could provide valuable insights into changes in ocean redox conditions, especially the development of PZE before the occurrence of terrestrial biomass.

This work is based on the previous detailed redox studies (Zhu et al., 2021b) and further applies Hg isotopic compositions to investigate the redox condition in the earliest Cambrian ocean in the Tarim basin. We further combined the biostratigraphic record to address the relationship between redox conditions, particularly the PZE, and the evolution of early animals.

2. Geological setting

The Tarim basin is one of the largest petroliferous basins in China and has undergone multiple sedimentary-tectonic cycles, including the late Neoproterozoic Rodinia supercontinent breaking up, the opening and closing of the paleo-Tethys during the Paleozoic – Mesozoic transition, and the Indo-Asian plate collision in the Cenozoic (Jia, 1997). Paleomagnetic data suggest that the Tarim block drifted from the margin of the Gondwana continent located between 0°N and 30°N (Li et al., 2008) (Fig. 1A), and gradually developed a passive continental margin at the northern edge of the Tarim Block during the Ediacaran - Cambrian (Jia, 1997). Palaeogeographic reconstructions suggests that the shallow-water platform developed to the west and deep-water basin developed to the east in the early Cambrian in the Tarim basin (Fig. 1B). With a global transgression, the siliciclastic – carbonate sedimentary succession of Yurtus Formation was widely deposited. A significant negative excursion of carbonate carbon isotope values recorded in the basal Yurtus Formation (Fig. 1C), which corresponds with the BACE (Zhu et al., 2006), could constrain the depositional age of the Yurtus Formation in the Tarim basin likely to between 542 Ma and 521 Ma (Yao et al., 2005).

Strata recovered by the X1 drillcore in the Aksu area were deposited in a mid-ramp setting in the northwestern Tarim Basin (Fig. 1B). The X1 drillcore recovers the Tonian-aged Aksu Group, Ediacaran Sugetbrak and Qigebrak formations, lower Cambrian Yurtus and Xiaoerbrak formations, in chronological order. The Aksu Group is the oldest crystalline basement in the Tarim basin, and comprises mainly metamorphic schist. The Sugetbrak Formation in X1 drillcore comprises a set of shallow-water siliciclastic deposits, mainly composed of muddy, fine-grained sandstone interbedded with sandy mudstone in the upper part, sandstone with sandy mudstone in the middle part, and conglomerate in the basal part. The Ediacaran Qigebrak Formation is composed of medium to thick-bedded dolostone. An unconformity surface was identified at the top of the Qigebrak Formation. This unconformity is widely developed in the northwestern Tarim basin and reflects the erosional effects of regression or uplift caused by the "Keping movement" (He et al., 2010). The Yurtus Formation overlies the Qigebrak Formation and consists of black shale with thin-bedded chert, dolostone, interbedded shale and dolostone, and black shale with thin-bedded phosphorite-bearing layers. The Xiaoerbrak Formation contains dolostone and the contact with the underlying Yurtus Formation is conformable.

3. Methods

All samples were prepared by removing the veins and crushed to 200 mesh. Total organic carbon (TOC) and total sulfur (TS) contents were analyzed on carbonate-free powders using a Leco CS-200 carbon-sulfur analyzer at Petroleum Geology Laboratory, China University of Petroleum.

Carbonate carbon and oxygen isotope compositions were analyzed using a Delta V Advantage isotope ratio mass spectrometer at the Laboratory Center, PetroChina Hangzhou Research Institute of Geology. The analytical precision of the $\delta^{13}C_{carb}$ and $\delta^{18}O_{carb}$ values is better than ±0.06 ‰ and ± 0.08 ‰, respectively. Organic carbon isotope compositions were measured using a Flash HT 2000 Plus and continuous-flow Delta V Advantage IRMS at China University of Geosciences. The analytical precision was better than 0.2 ‰ (1σ) for $\delta^{13}C_{org}$ based on replicate analyses of standards (USGS40 and IVA-Urea).

The Hg concentration was measured by Lumex RA-915 M. About 100 mg sample powder was placed in the sample vessel of PYRO-915+. Then, the powder was heated to 680–740 °C under pyrolysis, so that all forms of Hg in the sample are converted into elemental Hg(0). With a RA-915 M analyzer, the generated elemental Hg(0) was quantitatively determined on the basis of the absorption of 254 nm amplitude radiation by the mercury atomic vapor. The detection limit is 0.5–1 ppb. Duplicates were measured for each sample (relative standard deviation ≤5%). The international standard reference material NIST 1633c Coal Fly Ash

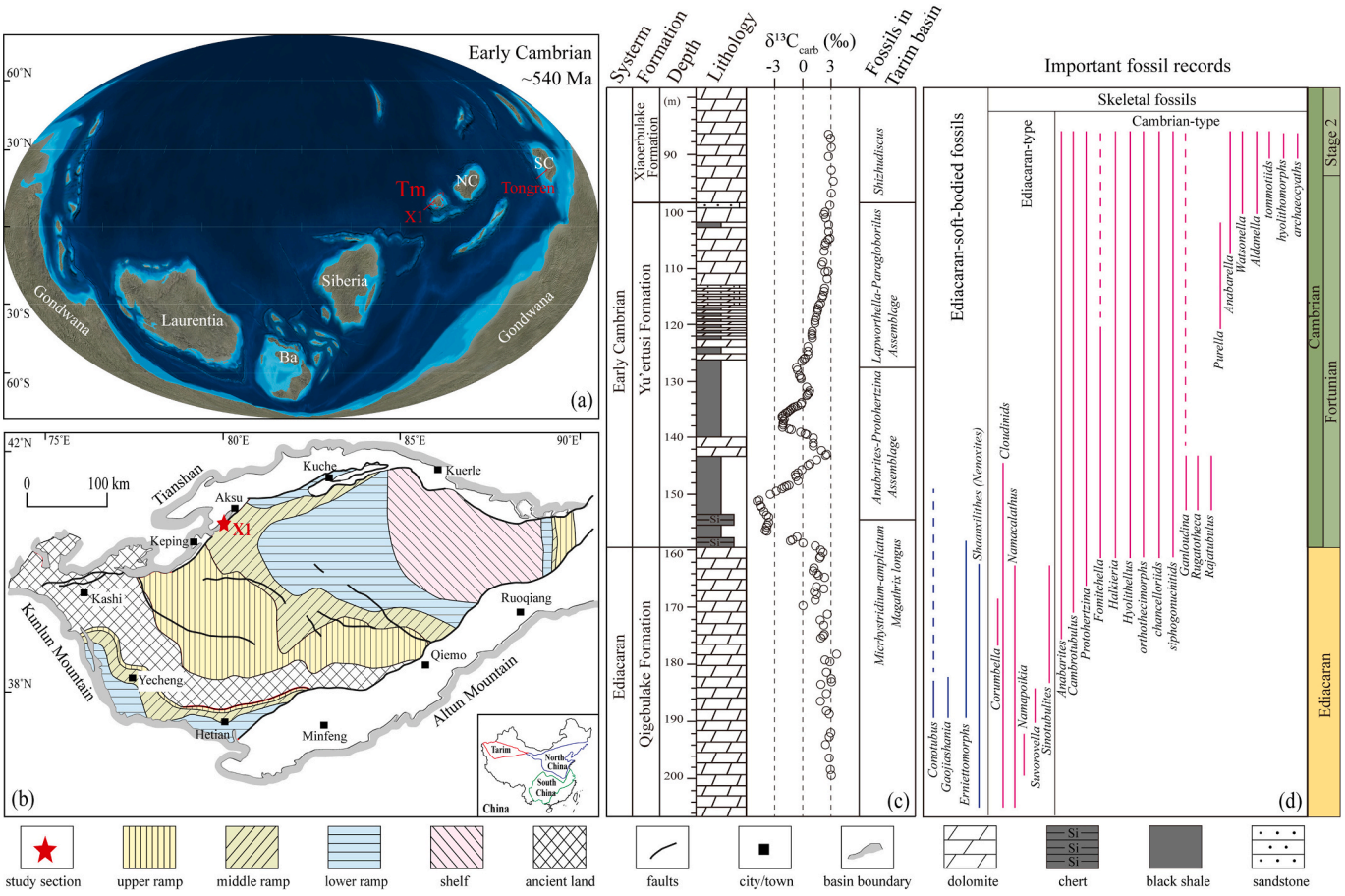

Fig. 1. (A) Global paleogeography of the early Cambrian (modified from https://deeptimemaps.com/). (B) Simplified map of reconstructed sedimentary environments of the early Cambrian Yurtus Formation (modified after Pan et al., 2015) and location of the study section (drill-core X1). (C) Stratigraphy and carbonate carbon isotope composition of drill-core X1. Fossils in Tarim basin modified after (Qian et al., 2009; Wu et al., 2021; Zhou, 2001). (D) Temporal distribution of Ediacaran-type soft-bodied and skeletal fossils and Cambrian-type skeletal fossils during the Ediacaran-Cambrian transition periods, modified after (Zhu et al., 2017). Ba—Baltica Block, Tm—Tarim Block, NC—North China Block, SC—South China Block.

(1005 ± 22 ppb) was used for generation of the standard curve (R2 ≥ 0.999) and quality control, and it was measured every 10 samples to monitor for signal stability.

Mercury stable isotopic composition was measured by multi-collector inductively coupled plasma mass spectrometry (MC-ICP-MS) at the State Key Laboratory of Environmental Geochemistry, Institute of Geochemistry, Chinese Academy of Sciences (IGCAS). The samples were pre-concentrated into 5 mL of a 40% mixed acid solution (*v*/v, HNO_3/HCl = 3/1) using a double-stage combustion protocol for Hg isotope analysis as previously described (Huang et al., 2016). NIST-3133 Hg standard and secondary standard solutions (UM-Almadén and NIST-3177) were prepared to match the Hg concentrations and matrix of sample solutions within 10%. The MDF of Hg isotopes is expressed in δ^{202}Hg (‰) and the calculation formula is as follows:

$$\delta^{202}\mathrm{Hg} = \left[\left({}^{202}\mathrm{Hg}/{}^{198}\mathrm{Hg}\right)_{\mathrm{sample}} \Big/ \left({}^{202}\mathrm{Hg}/{}^{198}\mathrm{Hg}\right)_{\mathrm{standard}} - 1\right] \times 1000 \quad (1)$$

MIF (Δ^{199}Hg, Δ^{200}Hg, Δ^{201}Hg) is calculated as follows:

$$\Delta^{199}\mathrm{Hg} \approx \delta^{199}\mathrm{Hg} - \delta^{202}\mathrm{Hg} \times 0.2520 \quad (2)$$

$$\Delta^{200}\mathrm{Hg} \approx \delta^{200}\mathrm{Hg} - \delta^{202}\mathrm{Hg} \times 0.5024 \quad (3)$$

$$\Delta^{201}\mathrm{Hg} \approx \delta^{201}\mathrm{Hg} - \delta^{202}\mathrm{Hg} \times 0.7520 \quad (4)$$

The UM-Almadén standard and NIST 3177 were used to determine the analytical accuracy of the isotopic analyses, and the isotopic ratios of δ^{202}Hg, Δ^{199}Hg, Δ^{200}Hg, and Δ^{201}Hg were similar to previously reported values. Data uncertainties (±2σ) reported here reflect the larger values of either the external precision of the replication of the standard solutions (UM-Almadén, NIST 3177 and GSS-4) or sample replicates.

4. Results

4.1. Carbonate and organic matter carbon isotope values ($\delta^{13}C_{carb}$ and $\delta^{13}C_{org}$)

Both $\delta^{13}C_{carb}$ and $\delta^{13}C_{org}$ values for X1 drillcore are presented in Supplementary Table S1. The Upper Qigebrak Formation show stable $\delta^{13}C_{carb}$ and $\delta^{13}C_{org}$ values, ranging from 0.01 to 3.54 ‰ and from −29.88 to −27.52‰, respectively. The Yurtus Formation show a coupled signature of $\delta^{13}C_{carb}$ and $\delta^{13}C_{org}$ values, implying that the organic carbon was derived from primary production (Jiang et al., 2012). For the sake of discussion, the Yurtus Formation was divided into four intervals (I, II, III, IV) according to the $\delta^{13}C_{carb}$ and $\delta^{13}C_{org}$ value (Fig. 2). Interval I is characterized by persistently negative $\delta^{13}C_{carb}$ and $\delta^{13}C_{org}$ values, vary from −4.02 to 1.83 ‰ and from −37.99 to −29.19 ‰, respectively. Interval II shows positive excursions in both $\delta^{13}C_{carb}$ (up to 2.50 ‰) and $\delta^{13}C_{org}$ (up to −26.43 ‰) values, but mild negative shift at the top. The $\delta^{13}C_{carb}$ and $\delta^{13}C_{org}$ values vary from −4.87 to 2.50 ‰ and from −38.49 to −26.43 ‰, respectively. The interval III represents the second, small negative carbon isotope excursion in the early Cambrian in Tarim basin, the $\delta^{13}C_{carb}$ values vary from −2.22 to 0.70 ‰

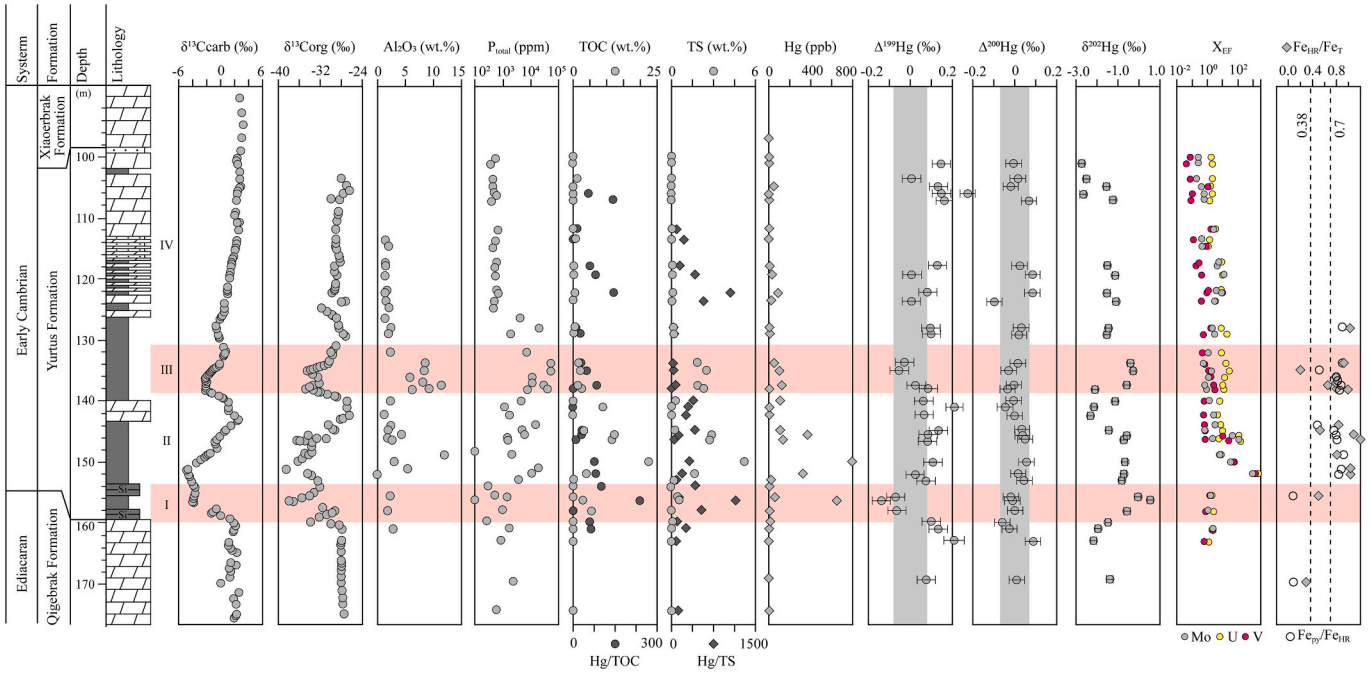

Fig. 2. Stratigraphic profiles of carbon isotopes, TOC, TS, Hg contents, and Hg isotopes for the Yurtus Formation. X_{EF} represent the trace element enrichment factors. The X_{EF} was calculated by the equation: $X_{EF} = [(X/Al)_{sample}/(X/Al)_{UCC}]$, where X (ppm) and Al (wt%) stand for their weight contents, and UCC stands for upper continental crust (Mo_{UCC} = 1.5 ppm, U_{UCC} = 2.8 ppm, Al_{UCC} = 8.04 wt%; McLennan, 2001). The Fe speciations modified after Zhu et al., 2021., where Fe_{HR}/Fe_T > 0.38 indicates anoxic conditions and Fe_{py}/Fe_{HR} > 0.7 indicates deposition under euxinic conditions. The gray band represents standard deviation of $\Delta^{199}Hg$ (± 0.08‰) and $\Delta^{201}Hg$ (± 0.06‰).

and the $\delta^{13}C_{org}$ values from −34.86 to −28.90 ‰. Interval IV shows a smooth positive shift of carbon isotope values, with the $\delta^{13}C_{carb}$ values varying from −0.72 to 2.86 ‰ and the $\delta^{13}C_{org}$ values from −31.73 to −26.36 ‰. The Xiaoerbrak Formation show steady $\delta^{13}C_{carb}$ values, range from 2.69 to 3.18 ‰, without $\delta^{13}C_{org}$ value.

4.2. Contents of total organic carbon (TOC) and total sulfur (TS)

The Qigebrak Formation show very low TOC and TS contents, the contents of TOC and TS vary from 0.00 to 1.15 wt% and from 0.01 to 0.03 wt%, respectively. The Yurtus Formation shows a wide range of TOC content from 0.01 wt% to 22.40 wt%, with an average of 2.8 wt% (n = 30). The TS content ranges from 0.01 wt% to 5.21 wt% with an average of 0.7 wt% (n = 32), and is positively correlated with TOC (Fig. 3, r = 0.79594, p < 0.01). The Xiaoerbrak Formation without the contents of TOC and TS.

4.3. Mercury contents and isotopic compositions

Samples of the Qigebrak Formation have low Hg concentrations, which range from 1.4 to 3.2 ppb. The three samples of the Qigebrak Formation show positive $\Delta^{199}Hg$ (0.07 to 0.20 ‰) and negative $\delta^{202}Hg$ values (−2.15 to −1.38 ‰), as well as invariable $\Delta^{200}Hg$ values (−0.02 to 0.09 ‰). Organic-rich sediments of the Yurtus Formation have a high Hg content (2.6 to 1689.5 ppb) and variable Hg isotopic compositions (Fig. 4a and b). Interval I is characterized by a negative shift of $\Delta^{199}Hg$ (from −0.14 to 0.10‰) and a positive shift in $\delta^{202}Hg$ values (from −1.47 to 0.55 ‰). Interval II is dominated by positive $\Delta^{199}Hg$ (0.02 to 0.21 ‰) and negative $\delta^{202}Hg$ values (−2.29 to −0.57 ‰). Interval III shows another negative shift of $\Delta^{199}Hg$ and a positive shift of $\delta^{202}Hg$, ranging from −0.05 to 0.08 ‰ and from −2.08 to −0.27 ‰. The interval IV records mostly positive $\Delta^{199}Hg$ (0.00 to 0.17 ‰) and slightly negative $\delta^{202}Hg$ values (−2.71 to −1.08 ‰). For even MIF of Hg isotopes, the $\Delta^{200}Hg$ shows an invariant trend for the Qigebrak and Yurtus formations. Overall, the Yurtus Formation show a strong negative correlation between $\Delta^{199}Hg$ and $\delta^{202}Hg$ (Fig. 4b, r = −0.767, p < 0.01).

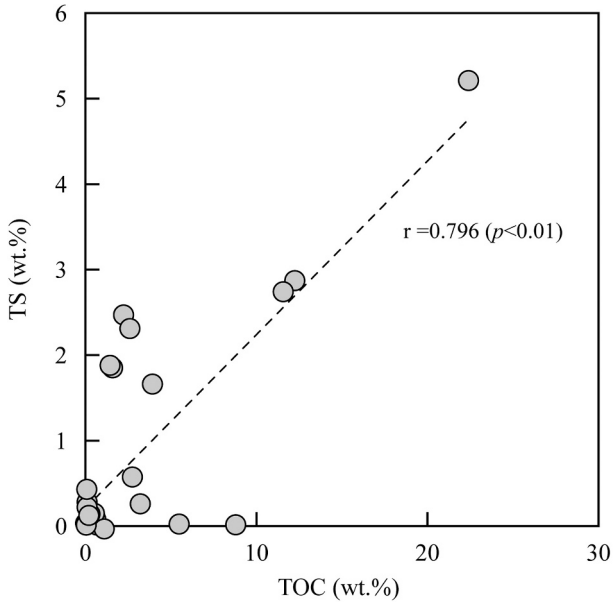

Fig. 3. The cross plot of TOC and TS of Yurtus Formation in X1 drill core.

5. Discussion

5.1. The host phases and sequestrations of Hg in the Yurtus Formation

Identifying the host phases of Hg in sediments is a critical procedure before applying Hg isotopes to track Hg sources. In general, organic matter is the main host phase of Hg in sediments (Ravichandran, 2004), however, Hg-sulfide complexes could become the main forms under

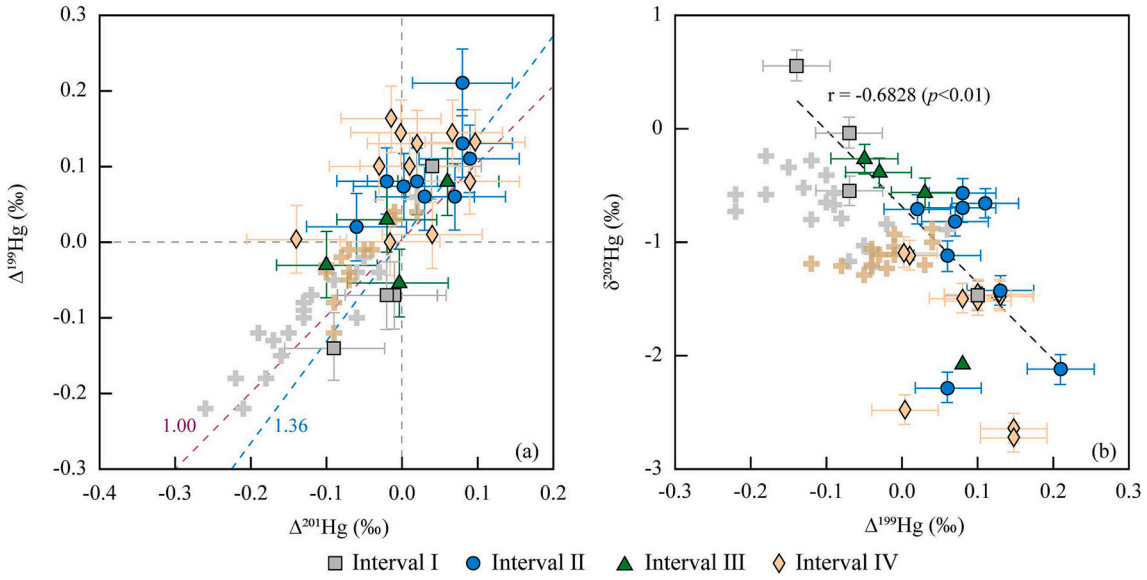

Fig. 4. The crossplots of $\Delta^{199}Hg$ vs $\Delta^{201}Hg$ values (a) and $\delta^{202}Hg$ vs $\Delta^{199}Hg$ values (b). The brown and gray crosses represent the Hg isotopic composition of the PZE in shallow and deep water environments during the Mesoproterozoic ocean, respectively (modified after Zheng et al., 2018). The linear correlation in (b) includes the all data of the Yurtus Formation. (For interpretation of the references to colour in this figure legend, the reader is referred to the web version of this article.)

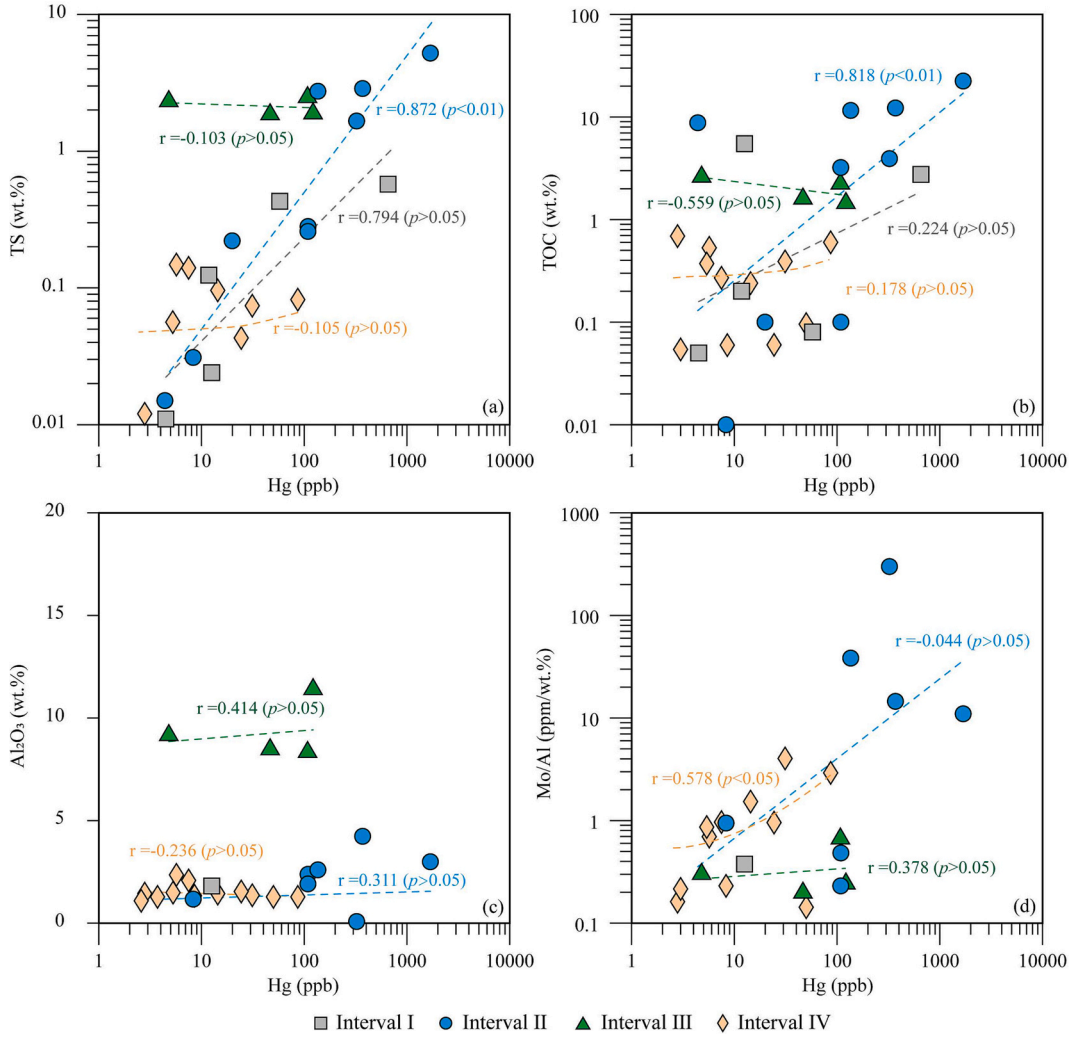

Fig. 5. The relationship between Hg content and TS, TOC, Al_2O_3 and a redox proxy Mo/Al.

euxinic conditions owing to the stronger affinity of Hg for sulfide (Sanei et al., 2012; Shen et al., 2019). Additionally, clay minerals and Mn-Fe-oxides (Kongchum et al., 2011) could also strongly control Hg sequestration from seawater. In the present study, a moderate correlation between Hg and TS was observed in interval I, suggesting sedimentary Hg is hosted by sulfide (Fig. 5a). A significant positive correlation was observed between Hg, and TS and TOC contents in interval II (Fig. 5a and b), suggesting that sedimentary Hg in interval II is mainly hosted by organic matter and sulfide. In contrast, neither TOC, TS, or Al_2O_3 show a correlation with Hg in interval III and IV (Fig. 5a, b, and c), which may suggest that other factors control Hg sequestration in these intervals.

Environmental changes (e.g. redox, sedimentation rate) can also affect Hg accumulation in sediments. High sedimentation rates tend to dilute and reduce Hg content in sediments while not affecting Hg burial flux (Bindler et al., 2001). Intensified anoxic conditions could promote Hg sequestration by enhancing organic matter or sulfide burial (Grasby et al., 2019). The lithology of Yurtus Formation is dominated by black shale (intervals I, II, and III) and carbonate (interval IV). Considering the faster precipitation of carbonate rocks, the sedimentation rate of black shale could be roughly constrained to 0.075–0.15 m/kyr (Zhu et al., 2021a), which is within the range of pelagic sedimentation rate of 0.005–0.25 m/kyr (Fairchild et al., 2016). Thus sedimentation rate is unlikely to be the dominant factor controlling Hg accumulation in the Yurtus Formation given the high Hg/TS and Hg/TOC ratios (Fig. 2). In fact, the similar lithologic variations suggest a consistent sedimentation rate for these intervals (I, II, and III). In such cases, Hg and metal elements still exhibit significantly different enrichments, which cannot be attributed to sedimentation rate variations, instead, elemental availability may dominate such stratigraphic variations (Zhu et al., 2021b). Alternatively, volcanic or hydrothermal activities could also result in high Hg/TOC or Hg/TS ratios (Grasby et al., 2019). This is because volcanic and hydrothermal activities can release large amounts of Hg in a short time. The high Hg/TOC and Hg/TS ratios in interval IV might be caused by very low TOC and TS contents, as well as high Hg contents (Table S1). Although interval I shows high Hg/TOC and Hg/TS ratios, and high Hg content, high Hg-MIF values were observed and therefore volcanic or hydrothermal fluxes can be ruled out because they have near-zero Δ^{199}Hg values (Blum et al., 2014; Sial et al., 2013). Additionally, a moderate correlation ($r = 0.578$, $p < 0.05$) between Hg and Mo/Al (a redox indicator, Algeo and Maynard, 2004) was observed in interval IV (Fig. 5d). This suggests that increased Hg contents were probably driven by enhanced euxinic conditions in this interval. Enhanced Hg sequestration in interval II could have also led to a depleted seawater Hg reservoir during deposition of the upper part of the Yurtus Formation, this mechanism is consistent with persistently positive $\delta^{13}C_{carb}$ and $\delta^{13}C_{org}$ values (Fig. 2).

5.2. *Mercury isotope composition record development and attenuation of PZE*

A significantly negative shift of Δ^{199}Hg (from 0.20 ‰ to −0.14 ‰) is observed in interval I of the Yurtus Formation (Fig. 2), along with a corresponding positive shift of δ^{202}Hg (from −1.47 ‰ to 0.55 ‰). This Hg isotope pattern is very similar to the one observed under PZE conditions during the Mesoproterozoic period (Fig. 4; Zheng et al., 2018). Previous experimental studies demonstrated that oceanic photoreduction of sulfur-bound Hg(II) produces negative MIF in the residual Hg(II), whereas Hg(II) bound to organic ligands (e.g., carboxyl ligand) typically generates positive MIF in the residual Hg(II) (Zheng and Hintelmann, 2010). PZE conditions would favor the binding of Hg(II) to sulfide and organic-reduced sulfur ligands, and thus result in negative MIF and positive MDF in the residual Hg(II) during photoreduction in the surface ocean, which could account for the negative shift of Δ^{199}Hg and the associated positive shift of δ^{202}Hg in the sediments of interval I. In addition, enhanced atmospheric Hg(0) sequestration under PZE into sediments was also hypothesized to cause a negative shift in Δ^{199}Hg value in euxinic conditions (Zheng et al., 2018). This is because modern atmospheric Hg(0) has a negative Δ^{199}Hg value (on average ~ −0.2 ‰; Demers et al., 2013) and the enriched thiol ligands and sulfide in the surface ocean under PZE conditions could enhance the oxidation of atmospheric Hg(0) in seawater (Zheng et al., 2019) and its subsequent sequestration to the sediments. This mechanism could also account for the negative correlation between Δ^{199}Hg and δ^{202}Hg because the aqueous oxidation of Hg(0) has been experimentally shown to produce positive δ^{202}Hg and negative Δ^{199}Hg in the oxidized phase (Hg(II)) (Zheng et al., 2019). The hypothesis of PZE in interval I is also supported by the presence of aryl isoprenoids (He et al., 2022; Li et al., 2021), a biomarker that indicates active green sulfur bacteria in the photic zone (Overmann and Tuschak, 1997). In addition, Fe speciation and Mo isotopes in our previous study also support an euxinic bottom water during the deposition of the Yurtus Formation (Zhu et al., 2021b). Nevertheless, there are other processes that could also lead to negative Hg-MIF in sediments, such as terrestrial input of Hg having negative Δ^{199}Hg values due to atmospheric Hg(0) accumulation in soils and vegetation (Shen et al., 2022). However, terrestrial soils and vegetation development before the Ordovician was very limited (Lenton et al., 2016). Therefore, the pattern of Hg isotope variations in interval I most likely records PZE.

Interval III shows a slight decline that gradually decreases to near-zero Δ^{199}Hg values that differ from the significant negative excursions in interval I (Fig. 2). In contrast to Hg(II) photoreduction in the PZE recorded by interval I, the gradually decreasing Δ^{199}Hg values from interval II (ranging from 0.02 to 0.21 ‰) to interval III (ranging from −0.05 to 0.08 ‰) might represent an enhanced terrestrial input of Hg (II). There are several lines of evidence to support this assumption. First, a gradual increase in Al_2O_3 content in interval III indicates the enhanced clay contribution (Fig. 2). Although soils and vegetation were limited before the Ordovician (Lenton et al., 2016), terrestrial Hg may have near-zero MIF, which is similar to the composition of silicate rocks (Fan et al., 2020). This enhanced Hg input from continental erosion could shift Δ^{199}Hg values from positive to near-zero in interval III. Second, sustained nutrient input could also stimulate increased primary productivity and changes in carbon burial, promoting microbial sulfate reduction and thus triggering the expansion of euxinic waters. This process is supported by the $\delta^{13}C_{carb}$ and $\delta^{13}C_{org}$ values and high TS contents of the interval (Fig. 2). Although sustained local volcanic Hg input can also lead to lower Δ^{199}Hg values because of near-zero Δ^{199}Hg values of local volcanic sources (Sial et al., 2013; Zambardi et al., 2009), no Hg enrichment, or Hg/TOC or Hg/TS spikes were observed (Fig. 2), and no volcanoes or tuff have been reported during the Lower Cambrian in the Tarim basin. On the other hand, previous study suggested euxinic bottom water in interval III based on the high Fe_{py}/Fe_{HR}, however, small near-zero Hg-MIF in this interval does not support photic zone euxinia, this suggests that H_2S-enrich bottom water is not expanding into the photic zone. Therefore, increased, terrestrial, Hg input associated with enhanced continental erosion probably drove the small shift of Δ^{199}Hg in interval III.

In contrast to intervals I and III, intervals II and IV show positive Δ^{199}Hg (0.02 ‰ to 0.21 ‰ and 0.00 ‰ to 0.17 ‰, respectively) along with negative δ^{202}Hg values (−2.29 ‰ to −0.57 ‰ and − 2.71 ‰ to −1.08 ‰, respectively), which are comparable to those of modern and ancient open ocean sediments (Štrok et al., 2015), where seawater Hg is primarily derived from atmospheric Hg (Grasby et al., 2017). The Hg isotope composition of intervals II and IV is also similar to modern ocean surface seawater (Jiskra et al., 2021). Intervals II and IV thus represent periods with attenuated PZE. The positive MIF in atmospheric Hg is likely derived from atmospheric photochemical reactions, which are thought to produce strong positive MIF signals in Hg(II), which dominates the Hg isotopic composition after deposition to the surface ocean (Jiskra et al., 2021). As a result, the dissolved Hg(II), which has a positive Δ^{199}Hg signature, complexes with sulfide or organic matter (Fig. 5a and b) and is recorded in sediments, like those deposited in the Ediacaran and Cambrian oceans (Fan et al., 2020; Yin et al., 2017).

Additionally, interval II shows no clearly high Hg/TOC or Hg/TS values, but extremely high TOC (up to 22.40 wt%) and TS (up to 5.21 wt%) and Hg (up to 1689.5 ppb) contents (Fig. 2), suggesting that Hg deposited from the atmosphere was accumulated in sediments via enhanced organic matter and/or sulfide sequestration. This process is also suggested by increasing $\delta^{13}C_{carb}$ and $\delta^{13}C_{org}$ values (Fig. 2). Conversely, interval IV has low TOC (the average is 0.38 wt%) and TS (the average is 0.05 wt%) contents, along with low Hg contents (the average is 18.8 ppb). Nevertheless, both intervals II and IV have similar Hg isotopic composition, which indicates enhanced sequestration of Hg(II) and records an attenuation of PZE. There are two samples in interval IV that have shown near-zero Δ^{199}Hg values, likely reflecting potential volcanic input (Sial et al., 2013; Zambardi et al., 2009). However, clear Hg anomalies were not identified based on Hg/TOC and Hg/TS values (Fig. 2). To sum up, the record of the stratigraphic variations in Hg isotope values confirms the development and decline of the PZE during the early Cambrian, which implies that the marine environment has gradually become habitable.

5.3. What triggered PZE?

PZE has been widely reported in modern and ancient oceans. In modern environments, PZE can develop in oxygen-minimum zones of oceans or in stratified basins (Arctic and Antarctic fjords, and Black Sea) (Brüchert et al., 2003; Smittenberg et al., 2004). In ancient oceans, PZE has also been widely reported from the Permian - Triassic mass

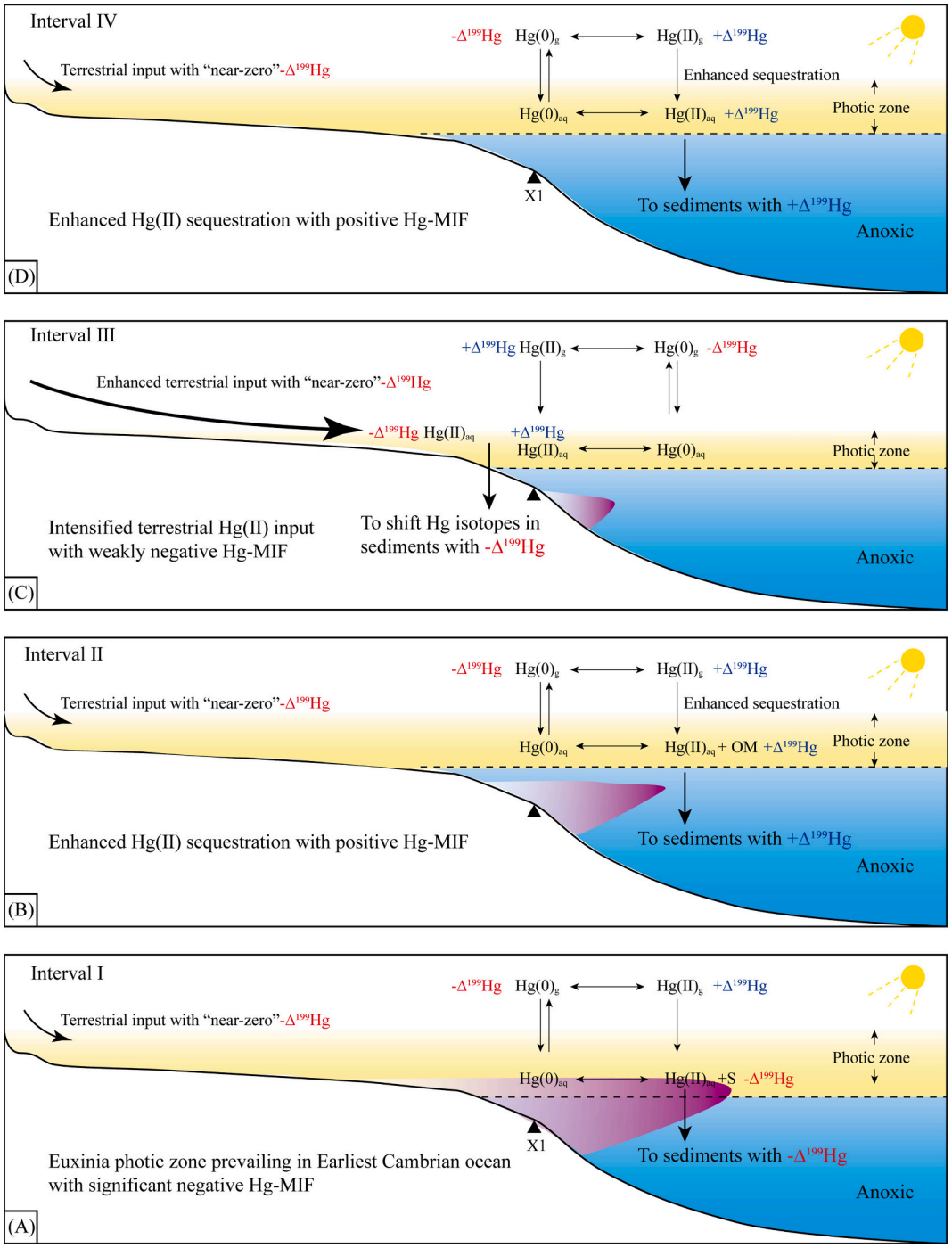

Fig. 6. Schematic diagram illustrating Hg cycles and PZE during the earliest Cambrian ocean.

extinction successions (Grice et al., 2005), the Late Devonian mass extinction successions (Kabanov and Jiang, 2020; Zheng et al., 2023a), and the Mesoproterozoic oceans (Zheng et al., 2018). It has been proposed that enhanced continental weathering through elevated nutrient input fluxes could trigger the expansion of PZE (Zhou et al., 2017). This hypothesis is based on the fact that high riverine nutrient fluxes would stimulate marine primary productivity and thus increase the consumption of oxygen, leading to the expansion of anoxia (Wei et al., 2020). Paleoceanographic model suggests that widespread oceanic anoxia and PZE could develop when riverine phosphate input reached ~10 times the modern value (Winguth and Winguth, 2012). Enhanced continental weathering occurred during the development of the great unconformity (Peters and Gaines, 2012), which is supported by rising $^{87}Sr/^{86}Sr$ values across the Ediacaran-Cambrian boundary (Shields, 2007; Stammeier et al., 2019). In the context of transgression, abundant nutrient and sulfate were transported to oceans, leading to intense bacterial sulfate reduction and enhanced H_2S production in the water column and hence the development of euxinic conditions in the photic zone of shelf areas (Fig. 6). This mechanism could also be generated by H_2S-enriched bottom water upwelling into shelf areas, leading to transient PZE. However, PZE may not have persisted for a long time. It can be roughly estimated that the PZE in Yurtus Formation would last approximately 26–53 ky based on the sedimentation rate and thickness. This is because of increased water column anoxia, which would have resulted in enhanced benthic regeneration of phosphorus from organic matter or iron oxyhydroxides (Van Cappellen and Ingall, 1994), which, in turn, stimulated surface primary productivity via positive feedback. The burial of organic matter and enhanced primary productivity would likely contribute to the atmospheric oxygen level (ρO_2) rise (Kump and Arthur, 1999). As a result, the redox chemocline moves down and H_2S in PZE would be oxidized to sulfate and returned to seawater reservoir, leading to the attenuation of PZE (Fig. 6).

5.4. Global or regional development of PZE?

By reevaluating previously published Hg isotope data during the early Cambrian, a distinct Hg-MIF was identified in the basal of the Niutitang Formation in South China (Tongren section). The $\Delta^{199}Hg$ value decreased from +0.15‰ to −0.18‰, whereas the $\delta^{202}Hg$ value increased from −4.03‰ to −0.78‰ (Zhu et al., 2021c). These significant concurrent negative Hg-MIF shift and positive Hg-MDF shift were more likely driven by photoreduction of Hg(II) under PZE conditions, which is similar to that of the late Mesoproterozoic (~ 1.1 Ga) ocean (Zheng et al., 2018), the Late Devonian ocean (Zheng et al., 2023a), and the Ediacaran ocean (Zheng et al., 2023b), as well as interval I of the Yurtus Formation. This proposed hypothesis was also supported by three main reasons. First, previous experimental studies have demonstrated that the photoreduction of Hg(II)-S results in an increase in $\delta^{202}Hg$ and a decrease in $\Delta^{199}Hg$ in residual Hg(II) stages (Motta et al., 2020; Zheng and Hintelmann, 2010), which is consistent with the trends exhibited in the Tongren section. Second, the direction and magnitude of $\Delta^{199}Hg$ and $\delta^{202}Hg$ of the Niutitang Formation in the Tongren section are strikingly similar to the Hg isotopic composition of three previously reported sections where PZE was independently validated. Third, the redox-sensitive element Mo exhibits moderate enrichment, indicating intermittent euxinia conditions (Zhu et al., 2021c). This is because molybdate (MoO_4^{2-}) is converted to thiomolybdate ($MoO_xS^{2-}_{[4-x]}$, x = 0 to 3) resulting in a highly enriched Mo in the sediment under the euxinic conditions (Erickson and Helz, 2000; Helz et al., 1996). Thus, multiple lines of evidence support that the Hg isotopic composition of the Niutitang Formation in the Tongren section records PZE in the earliest Cambrian ocean. The deposition age of the Niutitang Formation in the Tongren section is constrained to the bottom of the BACE period by a rough $\delta^{13}C_{carb}$ excursion (Fig. 7). In a word, Hg isotopic compositions from two different basins have shown the development of PZE during the early Cambrian. However, this does not mean that the PZE was widespread in

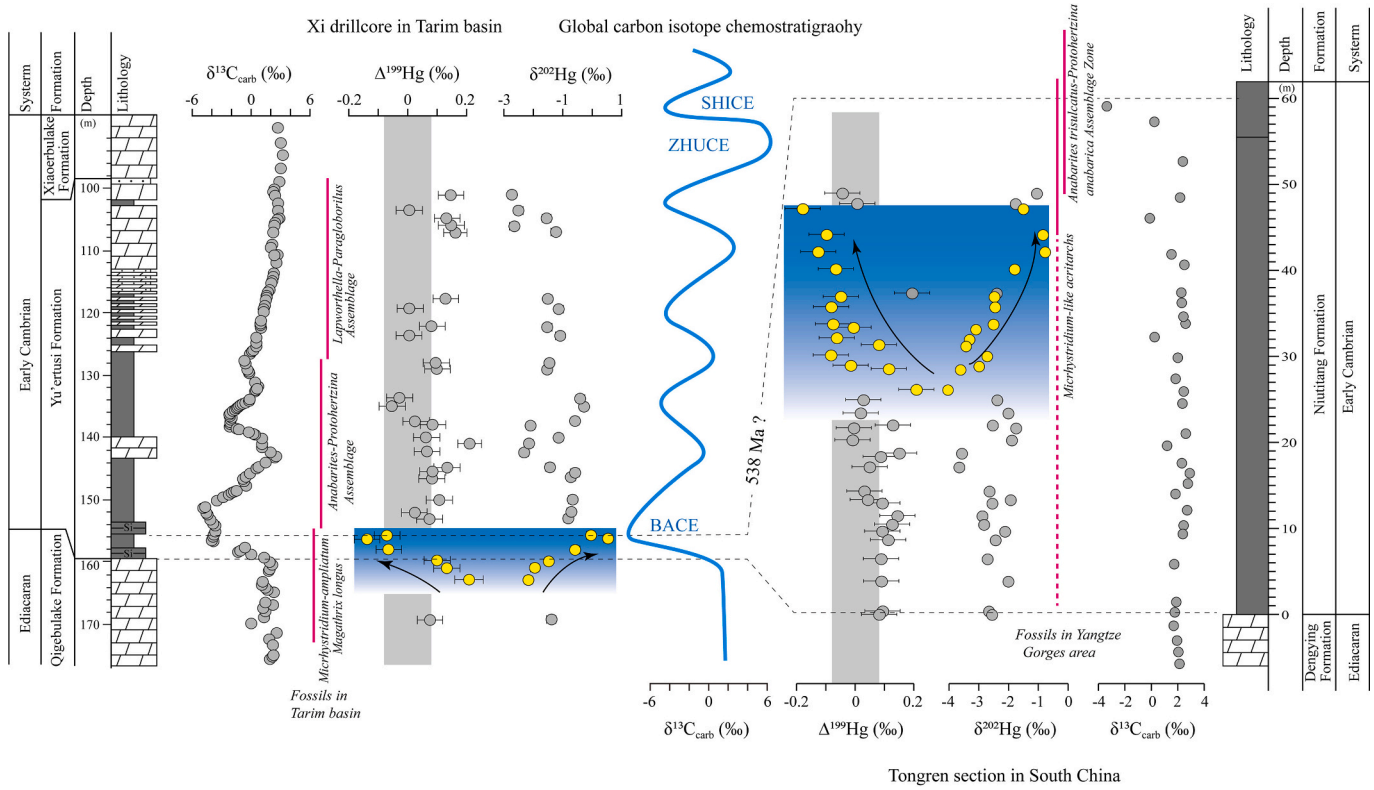

Fig. 7. Correlation of sections for Hg isotope compositions in Tarim basin and South China. The BACE curve is modified after (Zhu et al., 2007). Hg isotope composition of Tongren section in South China modified after (Zhu et al., 2021c), the fossils in Yangtze Gorges are is modified after (Jiang et al., 2012). The approximate paleogeographic location of the Tongren section is labeled in Fig. 1A.

the earliest Cambrian ocean. PZE should be strictly limited to nearshore environments, as the triggering of PZE requires large inputs of nutrients. Enhanced nutrient inputs elevate primary productivity while also increasing the availability of sulfate and organic matter for microbial sulfate reduction, resulting in the continued accumulation of seawater H_2S in the nearshore environment. Consequently, we suggest that PZE could develop in different basins when conditions are favorable but is definitely not prevalent in the entire basins.

5.5. Implications for marine environment and early animals

The Yurtus Formation shows significant negative Hg-MIF indicating PZE developed during interval I, enhanced Hg(II) sequestration in the interval II and IV, and intensified terrigenous input recorded in interval III, respectively. As a result, these Hg isotopes evidence indicate the development and attenuation of PZE during the earliest Cambrian oceans.

It has been long proposed that the establishment of early Earth ecosystem was benefited by co-evolution between marine environment and early animals (Erwin et al., 2011). Previous studies have proposed that the atmospheric oxygen level during the early Cambrian has reached 10% - 30% of the present atmospheric level (Mills et al., 2014), meaning an oxygenated ocean was probably present in the early Cambrian. However, multiple lines of evidence suggest that the O_2-deficient water column dominated the early Cambrian oceans, including Hg isotopes (this study), pyrite sulfur and iron isotopes (Xing et al., 2021), Fe speciation and redox-sensitive trace elements (Canfield et al., 2008), and Mo and U isotopes (Tostevin et al., 2019; Wen et al., 2015). The prevailing anoxic condition seems to contradict with the previous hypothesis that the rise of marine oxygen level led to the radiation of early animals in the early Cambrian. Following the extensive marine anoxia, the habitat of the early animals will be restricted to oxygen-rich shallow water areas if the global seafloor anoxia held within deep waters, and this could probably explain why the Nama biotic assemblage could thrive in well-oxygenated niches even though global anoxia was widespread (Tostevin et al., 2019, 2016; Wood et al., 2015). Nevertheless, most eukaryotic plankton inhabits the photic zone and thus PZE has been thought as an important kill mechanism for extinction. In a recent study, Zheng et al. (2023b) proposed a negative feedback of PZE on the marine environment and the biota by promoting anoxygenic photosynthesis and limiting the habitable space for eukaryotes. Given this mechanism, anaerobic photosynthesis overwhelmingly outcompetes aerobic photosynthesis when PZE develops. The aerobic eukaryotes would be forced further into the shallow oxygen-rich areas due to the decrease in oxygen availability. In addition, two negative Hg-MIF and positive Hg-MDF shifts interpreted as PZE are recognized in Tarim basin and Yangtze area, respectively (Fig. 7). The associated biostratigraphy record suggests that some Ediacaran-soft-bodied and Ediacaran-type skeletal fossils disappeared at PZE intervals (Fig. 1, e.g., *Shaanxilithes* and *Conotubus*). Furthermore, we compared the Hg isotopic composition and fossil records of the Yangtze Gorges area and Tarim basin, and it was striking that the Cambrian-type skeletal fossils (*Anabarites - Protohertzina Assemblage*) appeared after the negative Hg-MIF shift (Fig. 7). Even though this is not representative of the global fossil record, there is no doubt that PZE did have a negative impact on local biological evolution. Conversely, the attenuation of PZE indicates the removal of H_2S in the photic zone and the return of photosynthesis to aerobic dominance. This is followed by a rapid recovery of marine primary productivity and the accumulation of O_2 in surface seawater, further influencing the diversification and ecological expansion of early animals. Therefore, PZE may be one of the environmental factors for the Ediacaran – Cambrian biological transition.

6. Conclusion

In this study, we report the mercury isotopic composition of entire BACE events in the earliest Cambrian, Tarim basin, Western China. The results show that the development and decay of the PZE that recorded in the basal of the Yurtus Formation. The significant negative Hg isotopic shift at the basal of the Yurtus Formation records the occurrence of the PZE, where enhanced atmospheric Hg(0) deposition or sulfur-containing ligands of Hg(II) under PZE conditions leads to negative Hg-MIF in sediments. Instead, positive atmospheric oxidized Hg(II) deposition leads to a positive Hg-MIF in the sediments. Furthermore, we combined published Hg data in Yangtze area, which have shown similar Hg isotope compositions to the Tarim basin, suggesting the regional development of the PZE during the earliest Cambrian. Together with the biotic record, our results suggest that the development of PZE in the earliest Cambrian ocean may have significantly limited habitable space via H_2S poisoning. Conversely, the attenuation of the PZE would help to establish the habitable conditions for the diversification of early animals and pave the way for the early animal evolution.

Supplementary data to this article can be found online at https://doi.org/10.1016/j.gloplacha.2023.104214.

Declaration of Competing Interest

The authors declare that they have no known competing financial interests or personal relationships that could have appeared to influence the work reported in this paper.

Data availability

Data will be made available on request.

Acknowledgments

We would like to thank the two anonymous reviewers for their constructive comments, which have greatly improved the quality of the manuscript. This study is supported by the National Natural Science Foundation of China (42073068).

References

Algeo, T.J., Maynard, J.B., 2004. Trace-element behavior and redox facies in core shales of Upper Pennsylvanian Kansas-type cyclothems. Chem. Geol. 206, 289–318. https://doi.org/10.1016/j.chemgeo.2003.12.009.

Amthor, J.E., Grotzinger, J.P., Schröder, S., Bowring, S.A., Ramezani, J., Martin, M.W., Matter, A., 2003. Extinction of cloudina and namacalathus at the Precambrian-Cambrian boundary in Oman. Geology 31, 431–434. https://doi.org/10.1130/0091-7613(2003)031<0431:EOCANA>2.0.CO;2.

Bergquist, B.A., 2017. Mercury, volcanism, and mass extinctions. Proc. Natl. Acad. Sci. U. S. A. 114, 8675–8677. https://doi.org/10.1073/pnas.1709070114.

Bergquist, B.A., Blum, J.D., 2007. Mass-dependent and -independent fractionation of hg isotopes by photoreduction in aquatic systems. Science 318, 417–421.

Bindler, R., Renberg, I., Appleby, P.G., Anderson, N.J., Rose, N.L., 2001. Mercury accumulation rates and spatial patterns in lake sediments from West Greenland: a coast to ice margin transect. Environ. Sci. Technol. 35, 1736–1741. https://doi.org/10.1021/es0002868.

Blum, J.D., Bergquist, B.A., 2007. Reporting of variations in the natural isotopic composition of mercury. Anal. Bioanal. Chem. 388, 353–359. https://doi.org/10.1007/s00216-007-1236-9.

Blum, J.D., Sherman, L.S., Johnson, M.W., 2014. Mercury isotopes in earth and environmental sciences. Annu. Rev. Earth Planet. Sci. 42, 249–269. https://doi.org/10.1146/annurev-earth-050212-124107.

Bowyer, F.T., Zhuravlev, A.Y., Wood, R., Zhao, F., Sukhov, S.S., Alexander, R.D., Poulton, S.W., Zhu, M., 2023. Implications of an integrated late Ediacaran to early Cambrian stratigraphy of the Siberian Platform, Russia. GSA Bull. 1–23 https://doi.org/10.1130/b36534.1.

Brüchert, V., Jørgensen, B.B., Neumann, K., Riechmann, D., Schlösser, M., Schulz, H., 2003. Regulation of bacterial sulfate reduction and hydrogen sulfide fluxes in the central Namibian coastal upwelling zone. Geochim. Cosmochim. Acta 67, 4505–4518. https://doi.org/10.1016/S0016-7037(03)00275-8.

Canfield, D.E., Poulton, S.W., Narbonne, G.M., 2007. Late-Neoproterozoic deep-ocean oxygenation and the rise of animal life. Science 315, 92–95. https://doi.org/10.1126/science.1135013.

Canfield, D.E., Poulton, S.W., Knoll, A.H., Narbonne, G.M., Ross, G., Goldberg, T., Strauss, H., 2008. Ferruginous conditions dominated later Neoproterozoic deep-water chemistry. Science 321, 949–953.

Demers, J.D., Blum, J.D., Zak, D.R., 2013. Mercury isotopes in a forested ecosystem: Implications for air-surface exchange dynamics and the global mercury cycle. Glob. Biogeochem. Cycles 27, 222–238. https://doi.org/10.1002/gbc.20021.

Erickson, B.E., Helz, G.R., 2000. Molybdenum(VI) speciation in sulfidic waters: Stability and lability of thiomolybdates. Geochim. Cosmochim. Acta 64, 1149–1158. https://doi.org/10.1016/s0016-7037(99)00423-8.

Erwin, D.H., Laflamme, M., Tweedt, S.M., Sperling, E.A., Pisani, D., Peterson, K.J., 2011. The Cambrian conundrum: early divergence and later ecological success in the early history of animals. Science 334, 1091–1097. https://doi.org/10.1126/science.1206375.

Fairchild, I.J., Bonnand, P., Davies, T., Fleming, E.J., Grassineau, N., Halverson, G.P., Hambrey, M.J., McMillan, E.M., McKay, E., Parkinson, I.J., Stevenson, C.T.E., 2016. The late Cryogenian warm Interval, NE Svalbard: Chemostratigraphy and genesis. Precambrian Res. 281, 128–154. https://doi.org/10.1016/j.precamres.2016.05.013.

Fan, H., Fu, X., Ward, J.F., Yin, R., Wen, H., Feng, X., 2020. Mercury isotopes track the cause of carbon perturbations in the Ediacaran Ocean. Geology 49, 248–252. https://doi.org/10.1130/g48266.1.

Grasby, S.E., Shen, W., Yin, R., Gleason, J.D., Blum, J.D., Lepak, R.F., Hurley, J.P., Beauchamp, B., 2017. Isotopic signatures of mercury contamination in latest Permian oceans. Geology 45, 55–58. https://doi.org/10.1130/G38487.1.

Grasby, S.E., Them, T.R., Chen, Z., Yin, R., Ardakani, O.H., 2019. Mercury as a proxy for volcanic emissions in the geologic record. Earth-Sci. Rev. 196, 102880 https://doi.org/10.1016/j.earscirev.2019.102880.

Grice, K., Cao, C., Love, G.D., Böttcher, M.E., Twitchett, R.J., Grosjean, E., Summons, R. E., Turgeon, S.C., Dunning, W., Jin, Y., 2005. Photic zone euxinia during the permian-triassic superanoxic event. Science 307, 706–709. https://doi.org/10.1126/science.1104323.

He, J., Jia, C., Wu, G., Xu, B., 2010. Characteristics and model of Sinian weathering paleo-karst in Aksu area, Xinjiang. Acta Petrol. Sin. 26, 2513–2518.

He, T., Zhu, M., Mills, B.J.W., Wynn, P.M., Zhuravlev, A.Y., Tostevin, R., Pogge von Strandmann, P.A.E., Yang, A., Poulton, S.W., Shields, G.A., 2019. Possible links between extreme oxygen perturbations and the Cambrian radiation of animals. Nat. Geosci. 12, 468–474. https://doi.org/10.1038/s41561-019-0357-z.

He, T., Li, W., Lu, S., Pan, W., Ying, J., Zhu, P., Yang, E., Wang, X., Zhang, B., Sun, D., 2022. Mechanism and geological significance of anomalous negative δ13Ckerogen in the lower Cambrian, NW Tarim Basin, China. J. Pet. Sci. Eng. 208, 109384 https://doi.org/10.1016/j.petrol.2021.109384.

Helz, G.R., Miller, C.V., Charnock, J.M., Mosselmans, J.F.W., Pattrick, R.A.D., Garner, C. D., Vaughan, D.J., 1996. Mechanism of molybdenum removal from the sea and its concentration in black shales: EXAFS evidence. Geochim. Cosmochim. Acta 60, 3631–3642. https://doi.org/10.1016/0016-7037(96)00195-0.

Huang, Q., Chen, J., Huang, W., Fu, P., Guinot, B., Feng, X., Shang, L., Wang, Zhuhong, Wang, Zhongwei, Yuan, S., Cai, H., Wei, L., Yu, B., 2016. Isotopic composition for source identification of mercury in atmospheric fine particles. Atmos. Chem. Phys. 16, 11773–11786. https://doi.org/10.5194/acp-16-11773-2016.

Jia, C., 1997. Tectonic Characteristics and Petroleum, Tarim Basin, China. Geological Publishing House, Beijing.

Jiang, G., Wang, X., Shi, X., Xiao, S., Zhang, S., Dong, J., 2012. The origin of decoupled carbonate and organic carbon isotope signatures in the early Cambrian (ca. 542-520Ma) Yangtze platform. Earth Planet. Sci. Lett. 317–318, 96–110. https://doi.org/10.1016/j.epsl.2011.11.018.

Jiskra, M., Heimbürger-Boavida, L.E., Desgranges, M.M., Petrova, M.V., Dufour, A., Ferreira-Araujo, B., Masbou, J., Chmeleff, J., Thyssen, M., Point, D., Sonke, J.E., 2021. Mercury stable isotopes constrain atmospheric sources to the ocean. Nature 597, 678–682. https://doi.org/10.1038/s41586-021-03859-8.

Kabanov, P., Jiang, C., 2020. Photic-zone euxinia and anoxic events in a Middle-late Devonian shelfal sea of Panthalassan continental margin, NW Canada: changing paradigm of Devonian Ocean and sea level fluctuations. Glob. Planet. Chang. 188, 103153 https://doi.org/10.1016/j.gloplacha.2020.103153.

Kongchum, M., Hudnall, W.H., Delaune, R.D., 2011. Relationship between sediment clay minerals and total mercury. J. Environ. Sci. Heal. - Part A 46, 534–539. https://doi.org/10.1080/10934529.2011.551745.

Kump, L.R., Arthur, M.A., 1999. Interpreting carbon-isotope excursions: Carbonates and organic matter. Chem. Geol. 161, 181–198. https://doi.org/10.1016/S0009-2541(99)00086-8.

Laflamme, M., Darroch, S.A.F., Tweedt, S.M., Peterson, K.J., Erwin, D.H., 2013. The end of the Ediacara biota: Extinction, biotic replacement, or Cheshire Cat? Gondwana Res. 23, 558–573. https://doi.org/10.1016/j.gr.2012.11.004.

Lenton, T.M., Dahl, T.W., Daines, S.J., Mills, B.J.W., Ozaki, K., Saltzman, M.R., Porada, P., 2016. Earliest land plants created modern levels of atmospheric oxygen. Proc. Natl. Acad. Sci. U. S. A. 113, 9704–9709. https://doi.org/10.1073/pnas.1604787113.

Li, Z.X., Bogdanova, S.V., Collins, A.S., Davidson, A., De Waele, B., Ernst, R.E., Fitzsimons, I.C.W., Fuck, R.A., Gladkochub, D.P., Jacobs, J., Karlstrom, K.E., Lu, S., Natapov, L.M., Pease, V., Pisarevsky, S.A., Thrane, K., Vernikovsky, V., 2008. Assembly, configuration, and break-up history of Rodinia: a synthesis. Precambrian Res. 160, 179–210. https://doi.org/10.1016/j.precamres.2007.04.021.

Li, C., Shi, W., Cheng, M., Jin, C., Algeo, T.J., 2020. The redox structure of Ediacaran and early Cambrian oceans and its controls. Sci. Bull. 65, 2141–2149. https://doi.org/10.1016/j.scib.2020.09.023.

Li, F., Zhu, G., Lv, X., Zhang, Z., Wu, Z., Xue, N., He, T., Wang, R., 2021. The disputes on the source of Paleozoic marine oil and gas and the determination of the Cambrian system as the main source rocks in Tarim Basin (in Chinese abstract). Acta Petrol. Sin. 42, 1417–1436.

McLennan, S.M., 2001. Composition of the Upper Continental Crust Revisited: insights from sedimentary rocks. Geochem. Geophys. Geosyst. 2 https://doi.org/10.1180/minmag.1998.62a.2.182.

Mills, B., Lenton, T.M., Watson, A.J., 2014. Proterozoic oxygen rise linked to shifting balance between seafloor and terrestrial weathering. Proc. Natl. Acad. Sci. U. S. A. 111, 9073–9078. https://doi.org/10.1073/pnas.1321679111.

Motta, L.C., Kritee, K., Blum, J.D., Tsz-Ki Tsui, M., Reinfelder, J.R., 2020. Mercury isotope fractionation during the photochemical reduction of Hg(II) coordinated with organic ligands. J. Phys. Chem. A 124, 2842–2853. https://doi.org/10.1021/acs.jpca.9b06308.

Oren, A., Padan, E., Malkin, S., 1979. Sulfide inhibition of Photosystem II in cyanobacteria (blue-green algae) and tobacco chloroplasts. Biochim. Biophys. Acta 546, 270–279. https://doi.org/10.1016/0005-2728(79)90045-8.

Overmann, J., Tuschak, C., 1997. Phylogeny and molecular fingerprinting of green sulfur bacteria. Arch. Microbiol. 167, 302–309. https://doi.org/10.1007/s002030050448.

Peters, S.E., Gaines, R.R., 2012. Formation of the 'Great Unconformity' as a trigger for the Cambrian explosion. Nature 484, 363–366. https://doi.org/10.1038/nature10969.

Qian, Y., Feng, W., Li, G., Yang, A., Feng, M., Zhao, X., Xiao, B., 2009. Taxonomy and biostratigraphy of the early Cambrian univalved mollusc fossils from Xinjiang. Acta Micropalaeontol. Sin. 26, 193–210.

Ravichandran, M., 2004. Interactions between mercury and dissolved organic matter - a review. Chemosphere 55, 319–331. https://doi.org/10.1016/j.chemosphere.2003.11.011.

Sanei, H., Grasby, S.E., Beauchamp, B., 2012. Latest permian mercury anomalies. Geology 40, 63–66. https://doi.org/10.1130/G32596.1.

Shen, J., Algeo, T.J., Chen, J., Planavsky, N.J., Feng, Q., Yu, J., Liu, J., 2019. Mercury in marine Ordovician/Silurian boundary sections of South China is sulfide-hosted and non-volcanic in origin. Earth Planet. Sci. Lett. 511, 130–140. https://doi.org/10.1016/j.epsl.2019.01.028.

Shen, J., Yin, R., Zhang, S., Algeo, T.J., Bottjer, D.J., Yu, J., Xu, G., Penman, D., Wang, Y., Li, L., Shi, X., Planavsky, N.J., Feng, Q., Xie, S., 2022. Intensified continental chemical weathering and carbon-cycle perturbations linked to volcanism during the Triassic–Jurassic transition. Nat. Commun. 13, 1–10. https://doi.org/10.1038/s41467-022-27965-x.

Shields, G.A., 2007. A normalised seawater strontium isotope curve: possible implications for Neoproterozoic-Cambrian weathering rates and the further oxygenation of the Earth. eEarth 2, 35–42. https://doi.org/10.5194/ee-2-35-2007.

Sial, A.N., Lacerda, L.D., Ferreira, V.P., Frei, R., Marquillas, R.A., Barbosa, J.A., Gaucher, C., Windmöller, C.C., Pereira, N.S., 2013. Mercury as a proxy for volcanic activity during extreme environmental turnover: the Cretaceous-Paleogene transition. Palaeogeogr. Palaeoclimatol. Palaeoecol. 387, 153–164. https://doi.org/10.1016/j.palaeo.2013.07.019.

Smittenberg, R.H., Pancost, R.D., Hopmans, E.C., Paetzel, M., Sinninghe Damsté, J.S., 2004. A 400-year record of environmental change in an euxinic fjord as revealed by the sedimentary biomarker record. Palaeogeogr. Palaeoclimatol. Palaeoecol. 202, 331–351. https://doi.org/10.1016/S0031-0182(03)00642-4.

Stammeier, J.A., Hippler, D., Nebel, O., Leis, A., Grengg, C., Mittermayr, F., Kasemann, S. A., Dietzel, M., 2019. Radiogenic Sr and Stable C and O Isotopes across Precambrian-Cambrian transition in Marine Carbonatic Phosphorites of Malyi Karatau (Kazakhstan)—implications for paleo-environmental change. Geochem. Geophys. Geosyst. 20, 3–23. https://doi.org/10.1029/2018GC007767.

Štrok, M., Baya, P.A., Hintelmann, H., 2015. The mercury isotope composition of Arctic coastal seawater. Compt. Rendus Geosci. 347, 368–376. https://doi.org/10.1016/j.crte.2015.04.001.

Tostevin, R., Mills, B.J.W., 2020. Reconciling proxy records and models of Earth's oxygenation during the Neoproterozoic and Palaeozoic. Interf. Focus 10. https://doi.org/10.1098/rsfs.2019.0137.

Tostevin, R., Wood, R.A., Shields, G.A., Poulton, S.W., Guilbaud, R., Bowyer, F., Penny, A.M., He, T., Curtis, A., Hoffmann, K.H., Clarkson, M.O., 2016. Low-oxygen waters limited habitable space for early animals. Nat. Commun. 7 (12818), 1–9. https://doi.org/10.1038/ncomms12818.

Tostevin, R., Clarkson, M.O., Gangl, S., Shields, G.A., Wood, R.A., Bowyer, F., Penny, A. M., Stirling, C.H., 2019. Uranium isotope evidence for an expansion of anoxia in terminal Ediacaran oceans. Earth Planet. Sci. Lett. 506, 104–112. https://doi.org/10.1016/j.epsl.2018.10.045.

Van Cappellen, P., Ingall, E.D., 1994. Benthic phosphorus regeneration, net primary production, and ocean anoxia: a model of the coupled marine biogeochemical cycles of carbon and phosphorus. Paleoceanography 9, 677–692. https://doi.org/10.1029/94PA01455.

Wei, G.Y., Wei, W., Wang, D., Li, T., Yang, X., Shields, G.A., Zhang, F., Li, G., Chen, T., Yang, T., Ling, H.F., 2020. Enhanced chemical weathering triggered an expansion of euxinic seawater in the aftermath of the Sturtian glaciation. Earth Planet. Sci. Lett. 539, 116244 https://doi.org/10.1016/j.epsl.2020.116244.

Wen, H., Fan, H., Zhang, Y., Cloquet, C., Carignan, J., 2015. Reconstruction of early Cambrian Ocean chemistry from Mo isotopes. Geochim. Cosmochim. Acta 164, 1–16. https://doi.org/10.1016/j.gca.2015.05.008.

Winguth, C., Winguth, A.M.E., 2012. Simulating Permian-Triassic oceanic anoxia distribution: Implications for species extinction and recovery. Geology 40, 127–130. https://doi.org/10.1130/G32453.1.

Wood, R.A., Poulton, S.W., Prave, A.R., Hoffmann, K.H., Clarkson, M.O., Guilbaud, R., Lyne, J.W., Tostevin, R., Bowyer, F., Penny, A.M., Curtis, A., Kasemann, S.A., 2015. Dynamic redox conditions control late Ediacaran metazoan ecosystems in the Nama Group, Namibia. Precambrian Res. 261, 252–271. https://doi.org/10.1016/j.precamres.2015.02.004.

Wood, R., Liu, A.G., Bowyer, F., Wilby, P.R., Dunn, F.S., Kenchington, C.G., Cuthill, J.F. H., Mitchell, E.G., Penny, A., 2019. Integrated records of environmental change and evolution challenge the Cambrian Explosion. Nat. Ecol. Evol. 3, 528–538. https://doi.org/10.1038/s41559-019-0821-6.

Wu, Y.S., Wang, W., Jiang, H.X., Cui, Y., Zhao, R., Huang, Z. Bin, Yang, Z.L., Chen, Y.Q., 2021. Evolution patterns of seawater carbon isotope composition during the Cambrian and their stratigraphic significance. Geol. J. 56, 457–474. https://doi.org/10.1002/gj.3957.

Xing, C., Lang, X., Ma, H., Peng, Yang, Peng, Yongbo, Liu, Y., Wang, R., Ning, M., Cui, Y., Yu, X., Shen, B., 2021. Predominant microbial iron reduction in sediment in early Cambrian sulfidic oceans. Glob. Planet. Chang. 206, 103637 https://doi.org/10.1016/j.gloplacha.2021.103637.

Yao, J., Xiao, S., Yin, L., Li, G., Yuan, X., 2005. Basal Cambrian microfossils from the Yurtus and Xishanblaq formations (Tarim, North-West China): Systematic revision and biostratigraphic correlation of Micrhystridium-like acritarchs. Palaeontology 48, 687–708. https://doi.org/10.1111/j.1475-4983.2005.00484.x.

Yin, R., Xu, L., Lehmann, B., Lepak, R.F., Hurley, J.P., Mao, J., Feng, X., Hu, R., 2017. Anomalous mercury enrichment in early Cambrian black shales of South China: Mercury isotopes indicate a seawater source. Chem. Geol. 467, 159–167. https://doi.org/10.1016/j.chemgeo.2017.08.010.

Zambardi, T., Sonke, J.E., Toutain, J.P., Sortino, F., Shinohara, H., 2009. Mercury emissions and stable isotopic compositions at Vulcano Island (Italy). Earth Planet. Sci. Lett. 277, 236–243. https://doi.org/10.1016/j.epsl.2008.10.023.

Zhang, F., Xiao, S., Kendall, B., Romaniello, S.J., Cui, H., Meyer, M., Gilleaudeau, G.J., Kaufman, A.J., Anbar, A.D., 2018. Extensive marine anoxia during the terminal ediacaran period. Sci. Adv. 4, 1–12. https://doi.org/10.1126/sciadv.aan8983.

Zhang, F., Xiao, S., Romaniello, S.J., Hardisty, D., Li, C., Melezhik, V., Pokrovsky, B., Cheng, M., Shi, W., Lenton, T.M., Anbar, A.D., 2019. Global marine redox changes drove the rise and fall of the Ediacara biota. Geobiology 17, 594–610. https://doi.org/10.1111/gbi.12359.

Zheng, W., Hintelmann, H., 2010. Isotope Fractionation of Mercury during its Photochemical Reduction by Low-Molecular-Weight Organic Compounds. J. Phys. Chem. A 114, 4246–4253. https://doi.org/10.1201/b10195-26.

Zheng, W., Obrist, D., Weis, D., Bergquist, B.A., 2016. Mercury isotope compositions across north American forests. Glob. Biogeochem. Cycles 30, 1475–1492. https://doi.org/10.1002/2015GB005323.

Zheng, W., Gilleaudeau, G.J., Kah, L.C., Anbar, A.D., 2018. Mercury isotope signatures record photic zone euxinia in the Mesoproterozoic Ocean. Proc. Natl. Acad. Sci. U. S. A. 115, 10594–10599. https://doi.org/10.1073/pnas.1721733115.

Zheng, W., Demers, J.D., Lu, X., Bergquist, B.A., Anbar, A.D., Blum, J.D., Gu, B., 2019. Mercury Stable Isotope Fractionation during Abiotic Dark Oxidation in the Presence of Thiols and Natural Organic Matter. Environ. Sci. Technol. 53, 1853–1862. https://doi.org/10.1021/acs.est.8b05047.

Zheng, W., Gilleaudeau, G.J., Algeo, T.J., Zhao, Y., Song, Y., Zhang, Y., Sahoo, S.K., Anbar, A.D., Carmichael, S.K., Xie, S., Liu, C.Q., Chen, J., 2023a. Mercury isotope evidence for recurrent photic-zone euxinia triggered by enhanced terrestrial nutrient inputs during the late Devonian mass extinction. Earth Planet. Sci. Lett. 613, 118175 https://doi.org/10.1016/j.epsl.2023.118175.

Zheng, W., Zhou, A., Sahoo, S.K., Nolan, M.R., Ostrander, C.M., Sun, R., Anbar, A.D., Xiao, S., Chen, J., 2023b. Recurrent photic zone euxinia limited ocean oxygenation and animal evolution during the Ediacaran. Nat. Commun. 14, 3920. https://doi.org/10.1038/s41467-023-39427-z.

Zhou, Z., 2001. Stratigraphy of the Tarim Basin. Science Press.

Zhou, W., Algeo, T.J., Ruan, X., Luo, G., Chen, Z.-Q., Xie, S., 2017. Expansion of photic-zone euxinia during the Permian–Triassic biotic crisis and its causes: Microbial biomarker records. Palaeogeogr. Palaeoclimatol. Palaeoecol. 474, 140–151. https://doi.org/10.1016/j.palaeo.2016.06.027.

Zhu, M.Y., Babcock, L.E., Peng, S.C., 2006. Advances in Cambrian stratigraphy and paleontology: Integrating correlation techniques, paleobiology, taphonomy and paleoenvironmental reconstruction. Palaeoworld 15, 217–222. https://doi.org/10.1016/j.palwor.2006.10.016.

Zhu, M., Strauss, H., Shields, G.A., 2007. From snowball earth to the Cambrian bioradiation: Calibration of Ediacaran-Cambrian earth history in South China. Palaeogeogr. Palaeoclimatol. Palaeoecol. 254, 1–6. https://doi.org/10.1016/j.palaeo.2007.03.026.

Zhu, M., Zhuravlev, A.Y., Wood, R.A., Zhao, F., Sukhov, S.S., 2017. A deep root for the Cambrian explosion: Implications of new bioand chemostratigraphy from the Siberian Platform. Geology 45, 459–462. https://doi.org/10.1130/G38865.1.

Zhu, G., Li, T., Huang, T., Zhao, K., Tang, W., Wang, R., Lang, X., Shen, B., 2021a. Quantifying the Seawater Sulfate Concentration in the Cambrian Ocean. Front. Earth Sci. 9 https://doi.org/10.3389/feart.2021.767857.

Zhu, G., Li, T., Zhao, K., Li, C., Cheng, M., Chen, W., Yan, H., Zhang, Z., Algeo, T.J., 2021b. Mo isotope records from lower Cambrian black shales, northwestern Tarim Basin (China): Implications for the early Cambrian Ocean. GSA Bull. 1–12 https://doi.org/10.1130/b35726.1.

Zhu, G., Wang, P., Li, T., Zhao, K., Zheng, W., Feng, X., Shen, J., Grasby, S.E., Sun, G., Tang, S., Yan, H., 2021c. Mercury record of intense hydrothermal activity during the early Cambrian, South China. Palaeogeogr. Palaeoclimatol. Palaeoecol. 568, 110294 https://doi.org/10.1016/j.palaeo.2021.110294.